AGU PUBLICATIONS

JGR

Journal of Geophysical Research: Oceans

RESEARCH ARTICLE

10.1002/2017JC012900

Key Points:
- First climatic scale analysis of ENSO and surface radiative fluxes
- Investigated the surface wind divergence/convergence to shed light on the issue of causes for limiting eastward excursions of convection
- Established that models are not fully able to reproduce observed patterns of ENSO-related radiation budget variability

Correspondence to:
R. T. Pinker,
pinker@atmos.umd.edu

Citation:
Pinker, R. T., S. A. Grodsky, B. Zhang, A. Busalacchi, and W. Chen (2017), ENSO impact on surface radiative fluxes as observed from space, *J. Geophys. Res. Oceans, 122*, 7880–7896, doi:10.1002/2017JC012900.

Received 18 MAR 2017
Accepted 10 JUL 2017
Accepted article online 11 AUG 2017
Published online 17 OCT 2017

ENSO impact on surface radiative fluxes as observed from space

R. T. Pinker[1], S. A. Grodsky[1], B. Zhang[1,2], A. Busalacchi[3], and W. Chen[1]

[1]Department of Atmospheric and Oceanic Science, University of Maryland, College Park, Maryland, USA, [2]NOAA NCEP Environmental Modeling Center, College Park, Maryland, USA, [3]University Corporation for Atmospheric Research, Boulder, Colorado, USA

Abstract We investigate the impact of El Niño-Southern Oscillation (ENSO) on surface radiative fluxes over the tropical Pacific using satellite observations and fluxes derived from selected atmospheric reanalyses. Agreement between the two in this region is important because reanalysis information is frequently used to assess surface energy budget sensitivity to ENSO. We found that during the traditional ENSO, the maximum variance of anomalous incoming solar radiation is located just west of the dateline and coincides with the area of the largest anomalous SST gradient. It can reach up to 60 W/m^2 and lags behind the Niño3 index by about a month, suggesting a response to anomalous SST gradient. The magnitude of longwave anomaly is only half that large and varies in phase with the SST anomaly. Similar anomalies were derived from outputs: from the European Centre for Medium-Weather Forecasts Reanalysis Interim (ERA-I), from the Modern Era Retrospective Analysis version 2 (MERRA-2), from the NCEP/NCAR Reanalysis 1 (R1), and from the Japanese JRA55 reanalysis. Among the four reanalyses used, results from ERA-I are the closest to observations. We have also investigated the surface wind divergence/convergence and found that the main factor limiting eastward excursions of convection is the surface wind convergence. Due to the wind divergence pattern normally present over the eastern cold tongue, anomalous convection extends into the eastern equatorial Pacific only during the strongest warm events. Our analysis also considers the El Niño Modoki events, for which the radiation flux patterns are shifted westward following the SST pattern.

1. Introduction

The normal conditions over the tropical Pacific are strongly affected by what is known the "warm pool" region in the western part of the ocean. This creates a circulation pattern known as the "Walker Circulation" (entered the meteorological vocabulary in honor of Sir Gilbert T. Walker who perceived it while working in the British Meteorological Office in India). The tropical Pacific Walker Cell (PWC) describes a west to east air movement in the upper troposphere and east-to-west at the surface (the latter is also a part of the southeasterly "trade winds"). This conceptual loop (Figure 1) starts with rising motion in the western part and sinking air in the eastern part of the tropical Pacific. It contributes to normal weather conditions in the tropical Pacific: warm, wet weather in the western Pacific and cool, dry one in the eastern Pacific. Under certain conditions, the Walker Circulation can change, resulting in weakened surface winds allowing the warm water of the western part to propagate to the east, a situation known as El Niño. When the Walker Circulation is strong, resulting winds cause strong upwelling and lower temperatures in the eastern Pacific, a condition known as La Niña. Sir G. T. Walker introduced the concept of Southern Oscillation (SO) which describes a variation in sea level barometric pressure between observing stations at Darwin, Australia, and Tahiti. Monthly sea level pressure (SLP) data measured at these two sites are available from 1882 and served as a basis for formulating the (SO) concept [*Rasmusson and Carpenter*, 1982; *Philander*, 1990]. A Tahiti-Darwin Southern Oscillation Index (SOI) is provided by the Climate Analysis Center of the U.S. and is a standardized difference between the two barometric pressures. The disturbed pattern of rising and sinking motions during ENSO affects cloud distributions, which in turn, impact the *surface radiation budget*. As stated by *Mayer et al.* [2016], El Niño-Southern Oscillation (ENSO) events lead to strong anomalies of the atmosphere-ocean energy budget, not only in the tropical Pacific Ocean but also at global scale. They found that the surface heat flux plays an important role in regulating the tropical Pacific Ocean heat content (OHC) variability associated with ENSO. Therefore, reliable estimates of the surface components of ocean heat budget are important. In this study, we focus on the impact of the disturbed conditions on

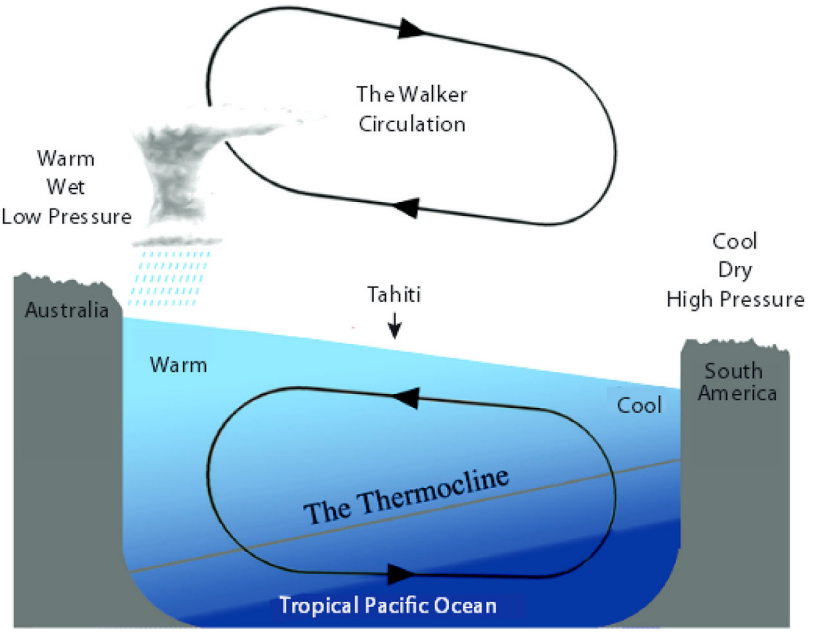

Figure 1. The Walker Circulation over the tropical Pacific Ocean. La Nina events modify the Walker Circulation and the thermocline will be displaced upward, reducing the depth of the cold waters. *From Wikipedia, the free encyclopedia.

the surface radiation field, a major component of the surface energy budget, which as yet, is not well known. While the impact of ENSO on the surface wind field was amply demonstrated, we provide independent evidence of the modification of the Walker Cell during El Niño and La Niña events as observed in surface radiative fluxes derived from space observations. We have also investigated to what extent selected well established reanalyses efforts can reproduce the observed patterns in surface radiative fluxes. We utilize the multivariate empirical orthogonal function (EOF) analysis involving anomalous sea surface temperature (SST), shortwave (SW↓) and longwave (LW↓) radiation, and surface wind divergence, to reveal some important features of the tropical convection response. We have also evaluated the relationship between the radiation fields in the tropical Pacific and SST, as well as relationships with various indices of ENSO such as Niño3 and the Modoki index (EMI) [*Ashok and Yamagata*, 2009]. Data used in this study are described in section 2, results are presented in section 3, and summary and discussion are presented in section 4.

2. Data Used

Data used in the analysis are summarized in Table 1. Additional details are as follows:

2.1. Satellite Based Estimates of Radiative Fluxes

Radiative fluxes (SW↓ and LW↓) for the area of interest come from the following sources:

a. Estimates based on observations provided by the International Satellite Cloud Climatology Project (ISCCP) version known as DX (pixel level sampled observations) [*Rossow and Schiffer*, 1991], using an inference scheme developed at the University of Maryland and labeled as UMD_ISCCP DX. The derived fluxes are gridded to 0.5° at 3 hourly time scale for July 1983 to December 2009 for SW↓ [*Ma and Pinker*, 2012] and at daily time scale for LW↓ [*Nussbaumer and Pinker*, 2012].

b. Estimates based on observation from the MODIS instrument, both on Terra and Aqua, using an inference schemes labeled as UMD_MODIS_SW↓ [*Wang and Pinker*, 2009] and UMD_MODIS_LW↓ [*Nussbaumer and Pinker*, 2012], both at daily time scale at 1° spatial resolution for the period of January 2002 to December 2012.

Table 1. Data Used

UMD/SRB DX (SW↓& LW↓)	0.5° × 0.5°	3-hourly	1983–2009
UMD/SRB MODIS (SW↓& LW↓)	1° × 1°	daily	2002–2012
ERA-I	0.75° × 075°	monthly	1981–2012
MERRA-2	1° × 1°	monthly	1981–2012
NCEP/NCAR Reanalysis R1	1.875°	monthly	1981–2010
JRA-55	1° × 1°	monthly	1981–2012

2.2. Reanalysis Data Used

a. ERA-Interim (ERA-I) [*Simmons et al*., 2007; *Berrisford et al*., 2009; *Dee et al*., 2011] (http://www.ecmwf.int/research/era). ERA-I is the latest global atmospheric reanalysis effort produced by the European Centre for Medium-Range Weather Forecasts (ECMWF).
b. The Modern Era Retrospective Analysis version 2 (MERRA-2) [*Bosilovich et al*., 2015] (https://gmao.gsfc.nasa.gov/reanalysis/MERRA-2/).
c. The Japanese 55-year reanalysis (JRA-55) [*Kobayashi et al*., 2015] (http://jra.kishou.go.jp/JRA-55/index_en.html).
d. The NCEP/NCAR Reanalysis (R1) product [*Kalnay et al*., 1996]. The main R1 products is archived at NCAR; the Earth System Research Laboratory's Physical Sciences Division of NOAA has the data in NetCDF format at http://www.esrl.noaa.gov/psd/.

2.3. Other Observational Data Used

Sea surface temperature data (SST) as provided by the NOAA Optimal Interpolation version 2 analysis (OIv2) [*Reynolds et al*., 2002] are used; they are available on a 1° × 1° grid since 1981. For surface winds, we rely on ERA-I and on the blended analysis of *Desbiolles et al*. [2017] that is available on a 1/4° grid, but only during 1992–2012.

3. Results

The two satellite SW↓ radiative flux products, namely, UMD_ISCCP DX and UMD_MODIS, have been merged as described in Appendix A. This merged product (to be labeled as UMD/SRB) is used in this study. The impact of merging on data quality was assessed by comparison to ground observations (Appendix A).

3.1. Selection of Disturbed Conditions Over the Tropical Pacific

The NOAA/National Weather Service, NOAA Center for Weather and Climate Prediction, Climate Prediction Center, provides information on the ENSO Index starting in 1950. The index is provided as an average for 3 months as follows: DJF, JFM, FMA, MAM, etc. Periods for investigating the impact of perturbed condition on radiative fluxes will be investigated for years of the strongest El Niño and La Niña conditions (during the period of available satellite data), namely, during 1987 and 1997 and 1988 and 2010, respectively (Table 2). As evident, the duration of perturbed conditions is not the same for each episode. The strong El Niño year of 1997 lasted from April to September with indices ranging from 0.7 to 2.3. The one during 1987 lasted the entire year with indices ranging from 1.0 to 1.6. The strongest La Niña occurred in 1988 between April and December with indices ranging between −0.8 and −1.9. The one during 2010 lasted from June to December with indices ranging between −0.09 and −1.5; the first 4 months of that year were under El Niño conditions. To put the selected cases in the context of other such conditions for the period of available satellite records, we show in Figure 2 time-longitude plots (*Hovmoller* representation) of equatorial anomalies (similar presentation for the years 1984–2000 can be found in *Rodriguez-Puebla et al*. [2008]). The strong control of the SST on the radiative fluxes is evident. During positive anomalies in SST, the SW↓ radiation decreases mostly, in the western part of the basin, while the positive anomalies in LW↓ coincide with those of the SST, indicating a strong impact of water vapor on the LW↓ fluxes [*Hall and Manabe*, 2000].

3.2. El Niño and La Nina Conditions

The 1987 El Niño case is illustrated in Figure 3 using SST, SW↓, and LW↓ anomalies simultaneously (the 1997 case of similar structure is not shown). During 1987, the January negative SW↓ anomaly in the Western Pacific is about −60 W/m^2 and is caused by the towering clouds in the warm pool region. It propagates toward the East, and by May, one can notice two centers, the strongest one around 129°W, slowly

Table 2. ENSO Index for Selected Years as Provided by the NOAA/National Weather Service, NOAA Center Weather and Climate Prediction Climate Prediction Center

1987	1.2	1.3	1.2	1.1	1.0	1.2	1.4	1.6	1.6	1.5	1.3	1.1
1988	0.8	0.5	0.1	−0.2	−0.8	−1.2	−1.3	−1.2	−1.3	−1.6	−1.9	−1.9
1997	−0.5	−0.4	−0.1	0.2	0.7	1.2	1.5	1.8	2.1	2.3	2.4	2.3
1999	−1.5	−1.3	−1.0	−0.9	−0.9	−1.0	−1.0	−1.1	−1.1	−1.3	−1.5	−1.7
2010	1.6	1.3	1.0	0.6	0.1	−0.4	−0.9	−1.2	−1.4	−1.5	−1.5	−1.5

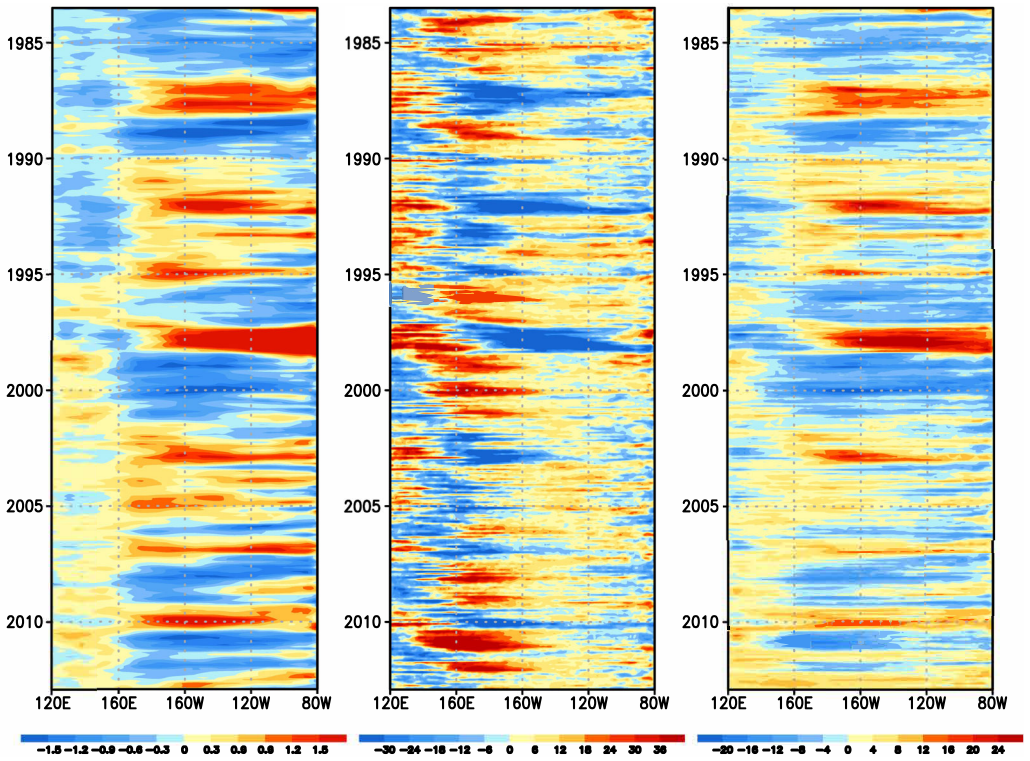

Figure 2. Time-longitude plot (*Hovmoller* representation) of equatorial monthly mean anomalies for (left) SST (°C); (middle) SW↓ (W/m^2); and (right) LW↓ (W/m^2) averaged over 5°S and 5°N.

weakening in the East and retreating back to the West. The largest positive anomaly of about 35 W/m^2 in the LW↓ during this El Niño period is situated closely over the SST anomaly and changes closely according to the pattern of the SST. It is caused by the simultaneous effect of clouds but dominated by water vapor which is a function of temperature and can be determined with the Clausius-Clapeyron relation [*Yau and Rogers*, 1989].

During the satellite record, the strongest La Niña occurred in 1988 lasting from April to December as illustrated in Figure 4. At the onset, we see a positive SW↓ anomaly in the Western part of the Pacific which intensifies with time, namely, decreased cloudiness in this part with an increase in the negative anomaly in the Eastern Pacific of about −40 W/m^2. A negative anomaly in LW↓ is covering most of the region and intensifying toward the West, positioned over the areas of a negative anomaly in SST, namely, reduction in cloudiness and water vapor during the colder sea surface temperatures.

The impact of ENSO on the direction and intensity of the wind field at the surface is well known. During El Niño periods, there is a weakening of the easterlies and at times, a reversal to westerlies is possible. We have investigated the monthly mean zonal wind anomalies using ERA-I data. As evident from Figure 5, during the 1987 El Nino, there is a strong positive anomaly in the horizontal wind speed centered over the warm pool area exceeding 6 m/s; this anomaly is reversed to negative values during the 1988 La Niña conditions.

In addition to the ENSO-induced response, the radiative flux snapshots of monthly anomaly patterns in Figures 3 and 4 contain significant transient variability, which is known to be present in the regional radiative and turbulent components of the heat flux [e.g., *Grodsky et al*., 2009]. To emphasize the portion of radiative flux variability associated with ENSO, we utilize the multivariate empirical orthogonal function (EOF) analysis involving anomalous SST, SW↓, LW↓, and surface wind divergence (Figure 6). The figure reveals some important features of the tropical convection response. Analysis of regional associations between SST and SW↓ suggests that anomalous tropical convection is not spatially linked to the region of anomalous SST maximum (Figures 6a and 6b). The above is associated with relatively cold equatorial SST in the east, which maintains high mean sea level atmospheric pressure and resulting low-level wind divergence

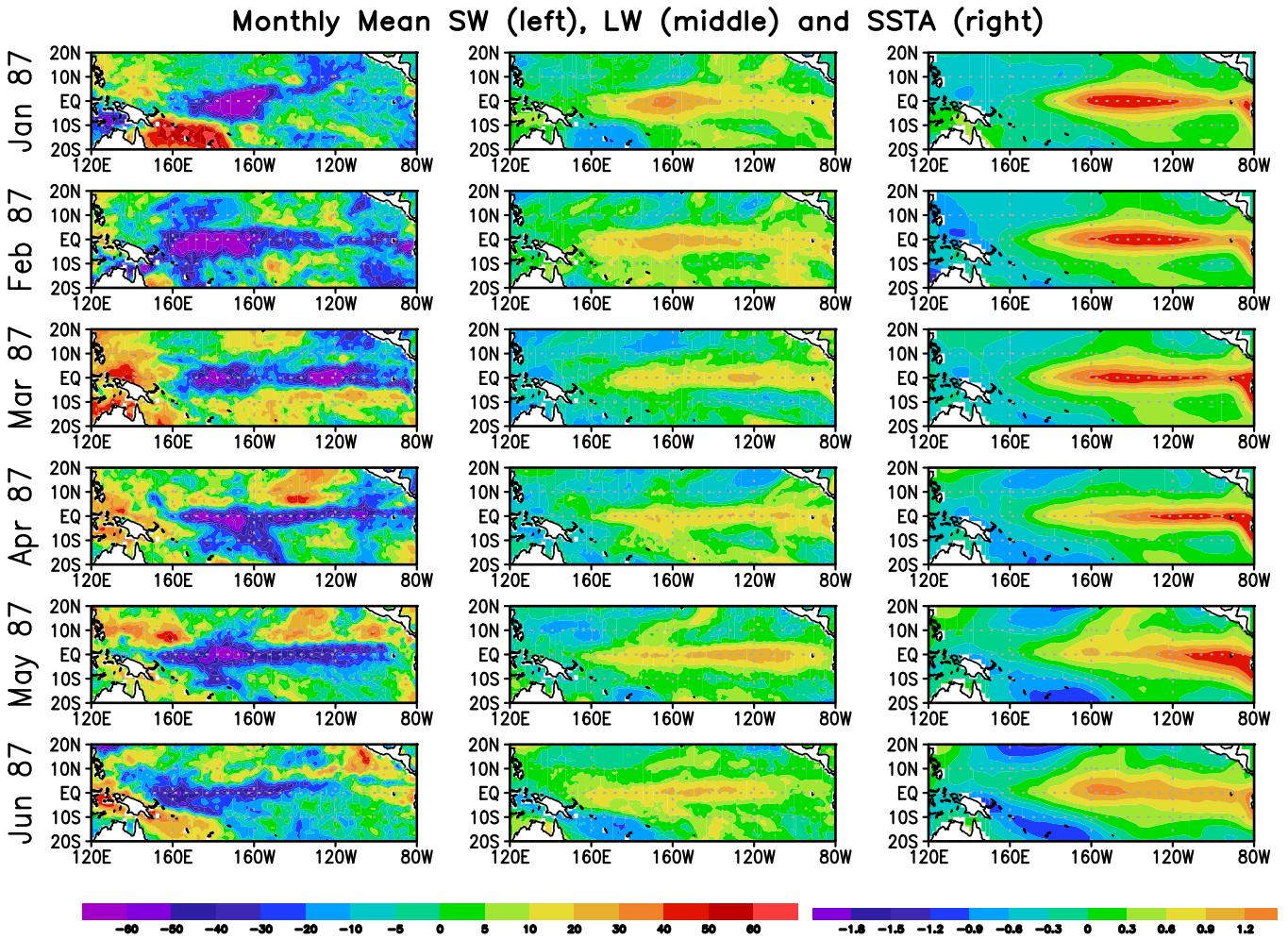

Figure 3. Evolution of monthly mean radiative flux anomaly and SST over the tropical Pacific during the 87 El Niño: (left) SW↓ fluxes W/m^2; (middle) LW↓ fluxes W/m^2; and (right) SST (8c).

over the cold tongue region. Even though the anomalous divU < 0 (Figure 6d) extends over the entire central and eastern equatorial Pacific, it overcomes the time mean eastern wind divergence (divU > 0) only during the strongest warm events (Figure 7a). Importantly, the anomalous divU pattern (Figure 6d) extends west beyond the date change line. The wind divergence pattern may be conditionally partitioned into two centers of action. In the east, the maximum magnitude of anomalous divU is associated with the local diabatic heating over anomalously warm SST [*Gill*, 1980]. In contrast in the west, the anomalous wind divergence is maintained by spatial changes in SST-induced atmospheric pressure gradient. In this region, this pressure gradient appears as the dominant driver of the local low-level atmospheric convergence leading to cumulonimbus convection accompanied by rainfall [*Lindzen and Nigam*, 1987]. Figure 6b suggests that local diabatic heating over anomalously warm SST in the east [*Gill*, 1980] is not enough to overcome the time mean divU > 0 over the cold tongue, except for the strongest warm events (Figure 7a). This convection limitation keeps the SW↓ pattern shifted to the west of the SST pattern. The maximum in the SW↓ attenuation is spatially collocated with the western edge of anomalous SST pattern (compare Figures 6a and 6b), just where the background easterly trade winds meet with the westerly flow anomaly forced by the westward SST-induced atmospheric pressure gradient.

Tropical convection has two major limiting factors: SST $> =27.5$°C and surface wind convergence, divU < 0. However, SST $> =27.5$°C is not sufficient for convection, and divU < 0 is closely associated with its presence or absence [*Graham and Barnett*, 1987]. In the tropical Pacific, both SST > 27.5°C and divU < 0 are present in the west, while colder SSTs and divergent winds dominate in the eastern cold tongue. These two imply that

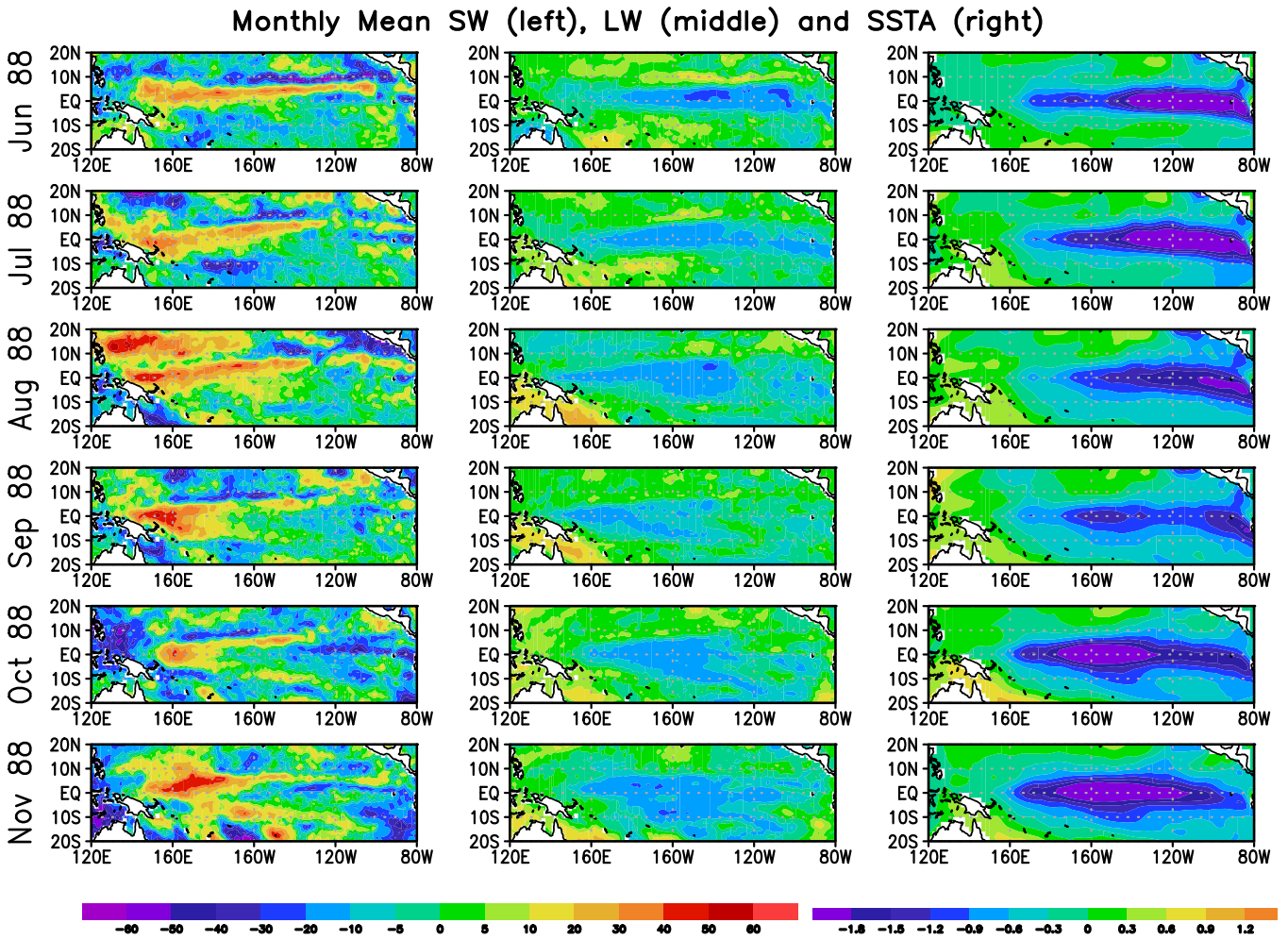

Figure 4. Evolution of monthly mean radiative flux anomaly over the tropical Pacific during the 88 La Niña. (left) SW↓ fluxes W/m^2; (middle) LW↓ fluxes W/m^2; and (right) SST (°C).

convection develops over the western equatorial Pacific. But it is not apparent a priori which factor (SST threshold or wind convergence) actually limits its eastern extent.

Downwelling shortwave radiation (SW↓) is normally high over the central equatorial Pacific. From the east, the area of high SW↓ is bounded by the stratus cloud deck over the cold tongue. From the west, the area of high SW↓ is bounded by a sharp zonal gradient associated with the western Pacific convection. Interannual zonal excursions of this sharp SW↓ gradient follow the eastern boundary of wind convergence while the 27.5°C isotherm is located about 1000 km to the east (Figure 7a). In that sense, the eastern boundary of the western equatorial Pacific convection is limited by the eastern boundary of the convection zone, divU < 0, rather than the western warm pool extent, SST $= 27.5$°C.

In addition to the time mean zonal shift between longitudes of SST $= 27.5$°C and divU $= 0$, their interannual variations (from corresponding time means) display similar correlation with the SOI and closely follow interannual variations of longitude of the maximum zonal gradient of SW↓ (Figure 7b). This suggests that the two longitudinal indices, lon (SST $= 27.5$°C) and lon (divU $= 0$), are equally appropriate for tracking the temporal part of the interannual displacements of the eastern boundary of the western Pacific convection zone, but only the second is also spatially collocated with the eastern edge of the convection zone.

In contrast with the SW↓, the spatial pattern of LW↓ response is closely tied with SST (Figure 6). Because the atmospheric humidity in the deep tropics is about saturated, the cloud cover does not have a strong effect on LW↓, which is governed by the atmospheric water vapor concentration [*Hall and Manabe*, 2000] that is

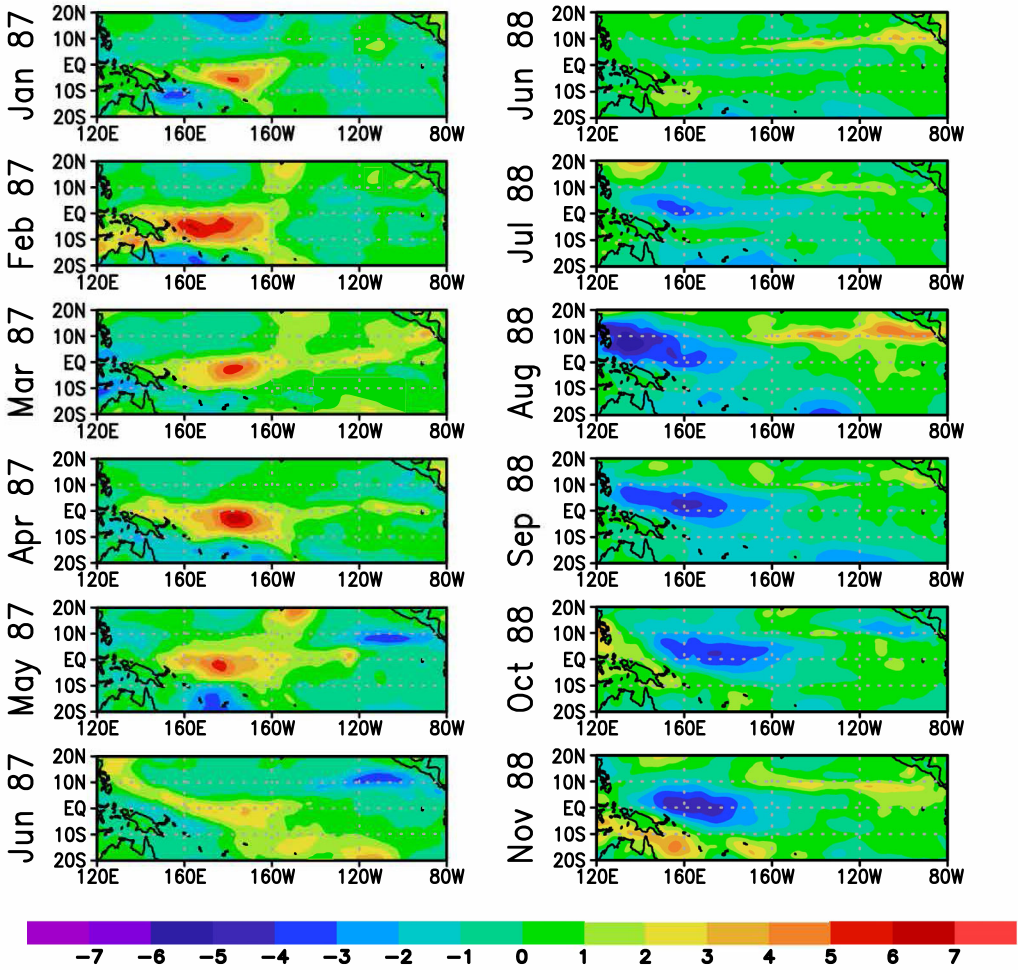

Figure 5. ERA-I monthly mean zonal wind anomaly during (left) El Nino and (right) La Nina.

closely linked with SST. That is why the LW↓ response pattern (Figure 6c) is apparently shifted eastward of the SW↓ pattern (Figure 6b) toward the core region of the SST pattern (Figure 6a). In addition to the difference in spatial patterns, the difference in the governing mechanisms account for the magnitude of ENSO-induced response that is almost two times larger for SW↓ than that for LW↓.

Atmospheric reanalyses are widely used as a proxy for observations. Therefore, we provide a brief evaluation of their performance in terms of ENSO-induced variations of surface radiative fluxes. Most of the modern reanalyses produce the correct zonal location of SW↓ pattern with a maximum spatially collocated with anomalous SST gradient in line with the *Lindzen and Nigam* [1987] mechanism. But all reanalyses produce a somewhat stronger SW↓ response in the east in comparison with observations. The closest correspondence with observations is produced by the ERA-I (compare Figures 8a, 8b, and 8i, 8j) while MERRA-2 slightly overestimates/underestimates SW↓/LW↓ response, respectively (Figures 8c and 8d). The strongest deviation from the observations is found for JRA55 that underestimates the magnitude of both radiative components by about 30% (Figures 8e and 8f). The patterns in Figure 8 are shown for illustration purposes and quantification of possible reasons for the deviation between ENSO-induced response in atmospheric reanalyses and observations is beyond the scope of this paper.

3.3. Correlation Between SW↓ and LW↓ Radiative Fluxes With El Niño Indices

Initially, we selected three indices, namely, Niño3, the Multivariate ENSO index (MEI) and the El Niño Modoki Index (EMI) to characterize ENSO. The Niño3 index is based on SST anomalies averaged over the region (5°N–5°S, 150°W–90°W) and is one of the oldest indices for monitoring ENSO [*Trenberth*, 1997; *Trenberth and Hoar*, 1996]. The MEI index is more comprehensive [*Wolter and Timlin*, 2011]; it is the first Principal

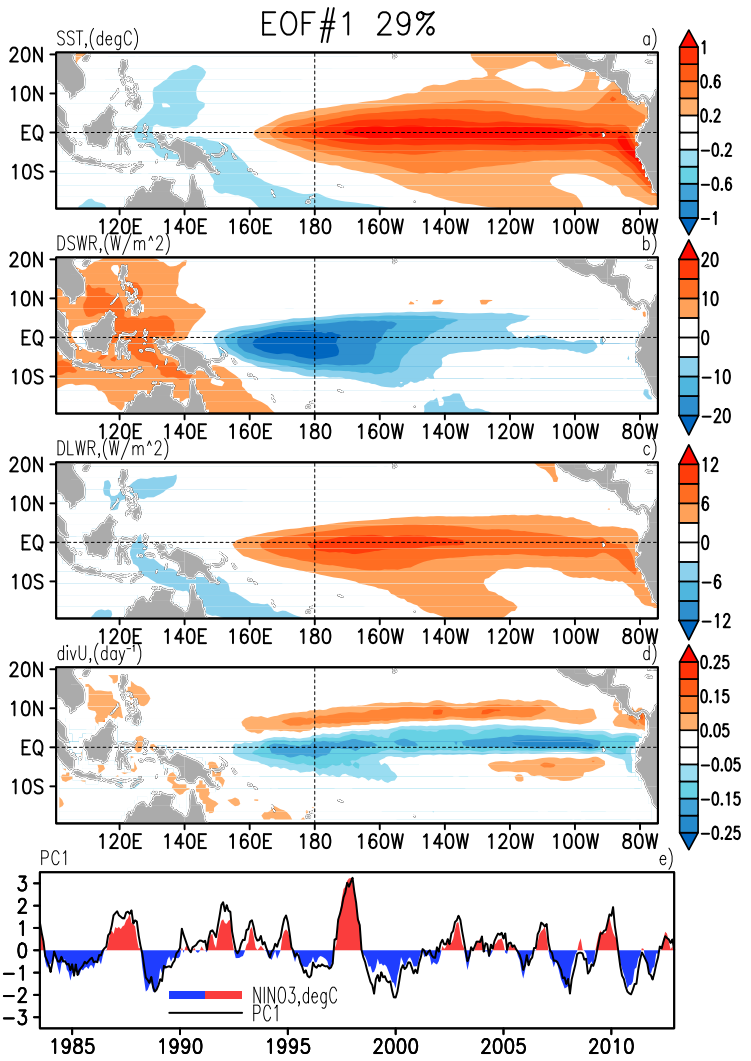

Figure 6. (a–d) Spatial and (e) temporal components of the leading four-variable EOF of observed monthly anomalous SST, SW↓, LW↓, and surface wind divergence (divU). Niño3 index is also shown (Figure 6e).

Component (PC) of the combined fields from six normalized meteorological and oceanographic variables: sea level pressure, zonal and meridional components of the surface wind, sea surface temperature, surface air temperature, and total cloudiness fraction. The EMI (Modoki) mode is the second EOF in an EOF analysis of SST anomalies over the tropical Pacific Ocean. The Modoki mode is different from the most dominant mode EOF1, which is related to traditional ENSO representation, like Niño3. EMI is defined as

$$\mathrm{EMI}=\mathrm{SSTA}_{(165^\circ\mathrm{E}-140^\circ\mathrm{W},\ 10^\circ\mathrm{S}-10^\circ\mathrm{N})}-0.5\mathrm{SSTA}_{(110^\circ\mathrm{W}-70^\circ\mathrm{W},\ 15^\circ\mathrm{S}-5^\circ\mathrm{N})}-0.5\mathrm{SSTA}_{(125^\circ\mathrm{E}-145^\circ\mathrm{E},\ 10^\circ\mathrm{S}-20^\circ\mathrm{N})}$$

to capture the zonal tripole pattern of Modoki mode [*Ashok et al.*, 2007]. The Modoki mode is associated with strong anomalous warming in the Central tropical Pacific and cooling in the Eastern and Western tropical Pacific. The teleconnections associated with this distinct warming and cooling patterns are very different from teleconnection patterns of the conventional El Niño. The term was introduced by T. Yamagata in 2004 to explain a probable cause behind the abnormal summer climatic conditions over Japan, speculating, that an increase in the sea surface temperature has activated convection currents and promoted a high-pressure ridge in the Pacific, bringing a hot summer to Japan ("Modoki" in Japanese means "similar but different"). *Yeh et al.* [2009] argue that an increasing frequency of the Modoki condition is due to anthropogenic warming, and that these events in the Central Pacific will occur more frequently if global warming occurs. The initial evaluation of these three indices has shown that the Nino3 and MEI behave similarly. As such, we will present results only for the other two (Figure 9).

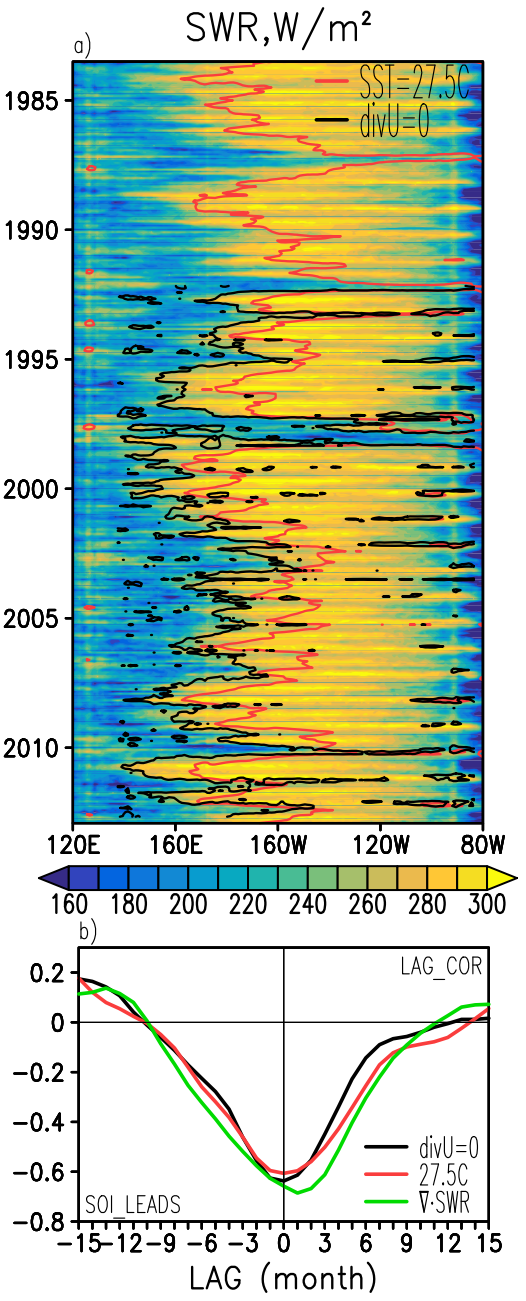

Figure 7. (a) Time-longitude plot (*Hovmoller* representation) of anomalous SW↓ (W/m^2) (SWR in figure) along the equator in the Pacific sector. Overlain contours are (black) divU = 0 (black) and SST = 27.5°C (red). (b) Lagged correlation of SOI with longitude of divU = 0 (black); SST = 27.5°C (red); and with the centroid of the eastward gradient of SWR (eastern boundary of the convection zone) (green).

We have investigated the lag correlation relationship of these ENSO indices with SW↓ and LW↓ fluxes. Lag correlation with a lag of ±15 months was calculated using both SW↓ and LW↓ fluxes with corresponding Niño3 and EMI indices, from July 1983 to December 2012. Lagged correlation shift of one time series by k months in time relative to another time series was computed. When considering two time series x and y of length N, the lag-correlation coefficients with k time-offset are

$$r_{xy}(k)=\frac{1}{N}\sum_{i=1}^{N-k}\frac{(x_i-\bar{x})(y_{i+k}-\bar{y})}{\sigma_x\ \sigma_y}\quad k=1\ \text{to}\ M$$

$$r_{xy}(k)=\frac{1}{N}\sum_{i=1-k}^{N}\frac{(x_i-\bar{x})(y_{i+k}-\bar{y})}{\sigma_x\ \sigma_y}\quad k=-(M-1)\ \text{to}-1$$

where M is maximum lag length, $\bar{x}$ and $\bar{y}$ are means, and σ_x and σ_y are standard deviations of x and y. The significance of lag-correlation coefficients can be tested with Student's *t* distribution with degrees of freedom N – 2 given as

$$t=r\sqrt{\frac{N-2}{1-r^2}}.$$

3.4. Correlation Between SW↓ and LW↓ Radiative Fluxes and Niño3

Figure 10 (left) displays the lag-correlation coefficients between Niño3 index with SW↓ flux anomalies from July 1983 to December 2012 along the equator from 120°E to 80°W for lead-lag times ranging from minus 15 months to plus 15 months. The very strong negative correlation exists from minus 4 months to plus 4 months, with the strongest correlation at plus 1 month. This means that Niño3 index leads SW↓ flux by about 1 month. The warm (cold) sea surface temperature over Niño3 region enhances (suppresses) convection and results in more (less) cloud cover which impacts the SW↓ flux reaching the surface. The most significant correlation (significance level of over 99.9%) is located near 165°W along the Pacific Equator. The lag-correlation coefficients between LW↓ fluxes and Niño3 (Figure 10, right) indicate that Niño3 leads LW↓ flux by 1 month and that the correlation center (significance level of over 99.9%) is at 150°W along the equatorial Pacific Ocean, namely, the LW↓ center is located 15° west of SW↓ Niño3 most significant correlation center.

3.5. Correlation Between SW↓ and LW↓ Radiative Fluxes and EMI

The lag correlation of EMI index with SW↓ flux anomalies is shown in Figure 11 (left). The most significant center (significance level of over 99.9%) is located near 165°E along the equatorial Pacific Ocean, which is 30° west of Niño3 peak correlation center and lags behind SW↓ flux by 1 month. The lag-correlation

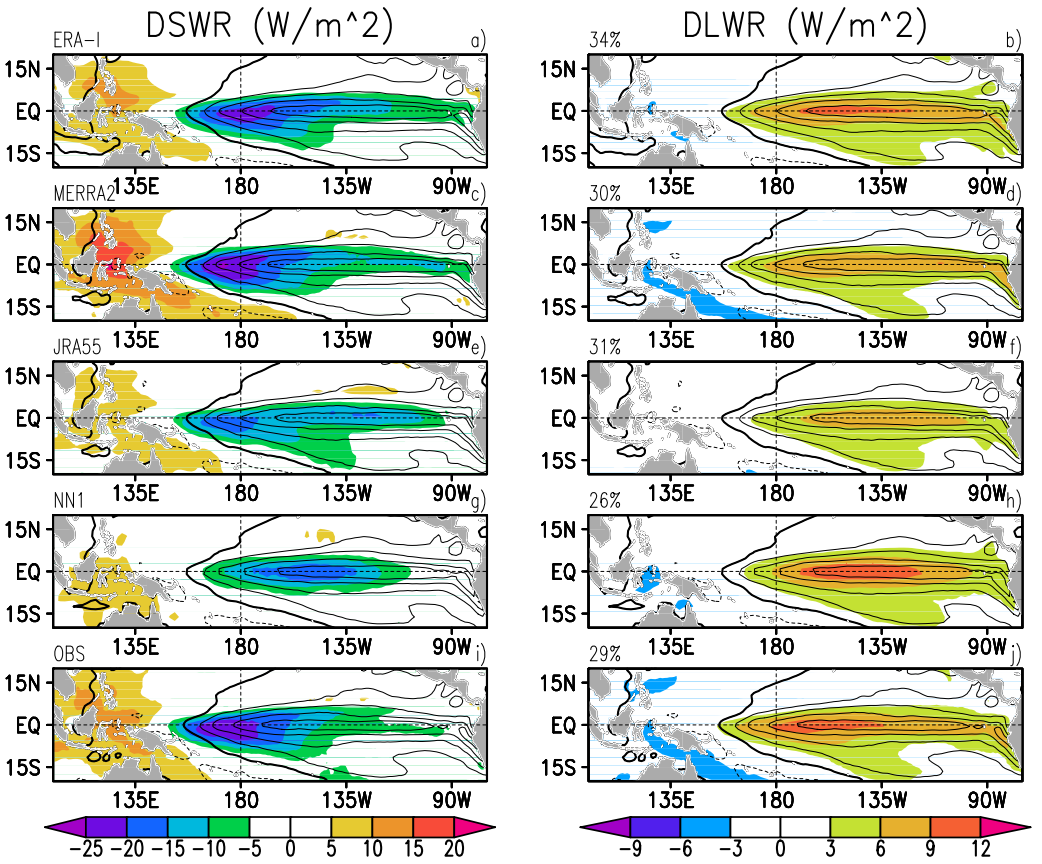

Figure 8. Spatial components of the leading trivariable EOF of monthly anomalous SST (contours, zero is bold, CI = 0.25 C), downwelling shortwave (SW↓ in W/m^2, left, shaded), and downwelling longwave (LW↓ in W/m^2, right, shaded) radiation from different atmospheric reanalyses. Percentage of explained variance is shown in the right column. For comparisons, the bottom line shows the leading trivariable EOF from our observations (a variant of what is shown in Figure 6).

coefficients between EMI and LW↓ flux is shown in Figure 11 (right). The LW↓ flux leads the EMI index by 1 month. The highest correlation centers at 165°E along the equatorial Pacific Ocean (significance level of over 99.9%). For EMI, both SW↓ and LW↓ center are at the same location, but LW↓ is 15° west of SW↓ for MEI and Niño3 indices. The physics behind the phenomena needs to be better understood.

3.6. Time Series at Locations of Highest Lag Correlations

Time series of detrended SW↓ and LW↓ flux anomalies and the ENSO indices are shown in Figures 12 and 13. As discussed earlier, the time series are illustrated for the location of highest correlation for the particular radiative flux component. As shown in Figure 10 for the Niño3 index, it is at 0, 165°W for SW↓ (Figure 10, left) and at 0, 150°W for LW↓ (Figure 10, right). The correlation between Nino3 and the SW↓ is −0.63 (significance level of over 99.9%) (Figure 12a), while the correlation with the LW↓ is 0.81 (significance level of over 99.9%) (Figure 12b), which is stronger than the SW↓. Similar correlations (at same as above significance levels) are shown in Figure 13 for detrended time series of UMD/SRB SW↓ and LW↓ flux anomalies and EMI Index.

4. Discussion and Summary

The Walker Circulation is of significance in weather and climate due to its large span of influence. The warm waters of the western Pacific Ocean supply the air with moisture forming clouds; the air then flows across the Pacific to the east and sinks at the west coast of South America, completing a loop by returning back to the western Pacific Ocean along the surface. In addition to the zonal circulation of the Walker Cell, the heating of the tropics creates a meridional circulation known as the Hadley Circulation. Their combined effects alter the sources of atmospheric heating affecting atmospheric circulation and climate at global scale [*Oort*

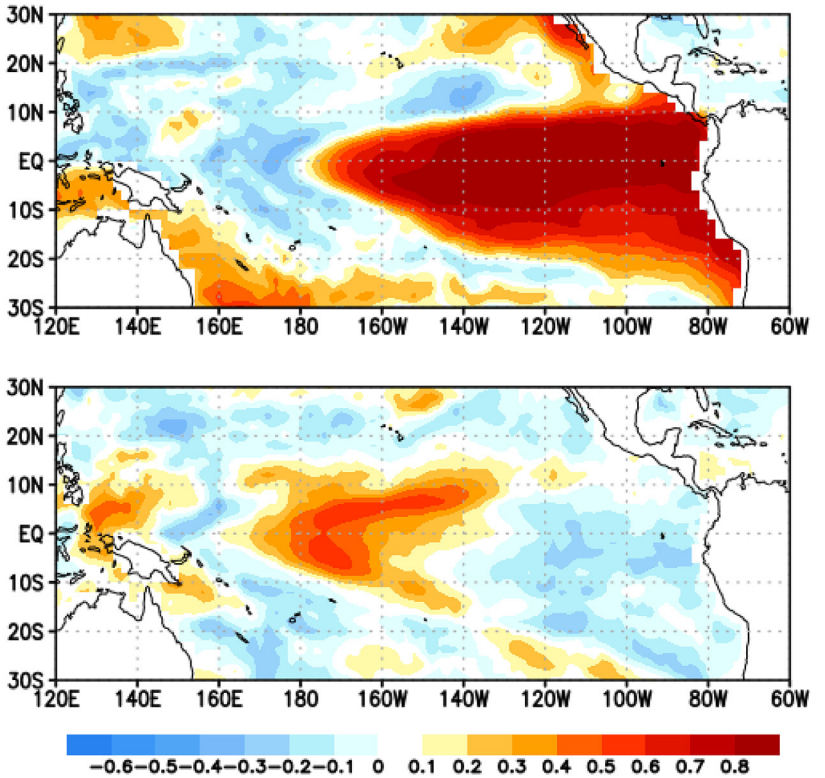

Figure 9. Correlation between selected ENSO indices and sea surface temperature. (top) Niño3 and (bottom) Modoki (EMI).

and Yienger, 1996; *Klein et al*., 1999]. The impact of the Walker Circulation results in the modification of wind patterns which in extreme cases, can lead to a full directional reversal. Surface heating, cloud formation, and moisture distribution are also modified, impacting surface radiative fluxes. Using satellite observations,

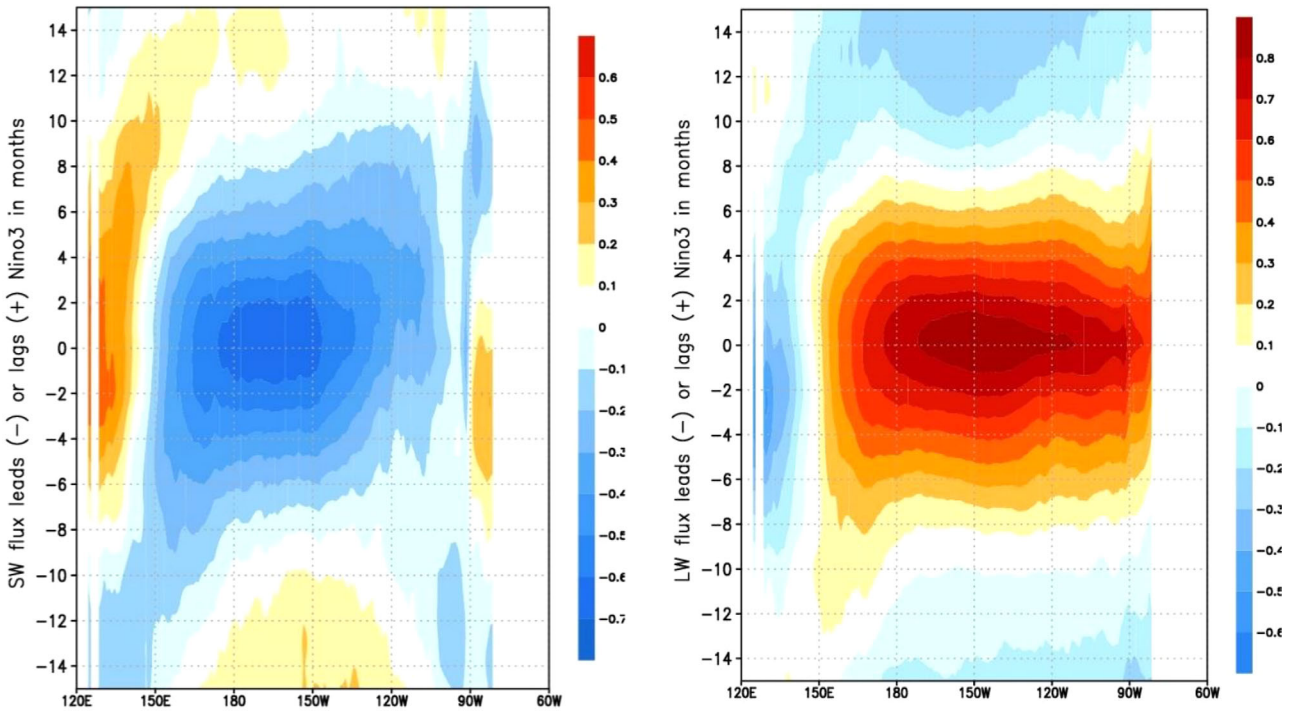

Figure 10. Lag cross correlations between Niño3 Index and SW↓ and LW↓ radiative fluxes during the period July 1983 to December 2012 along the equator.

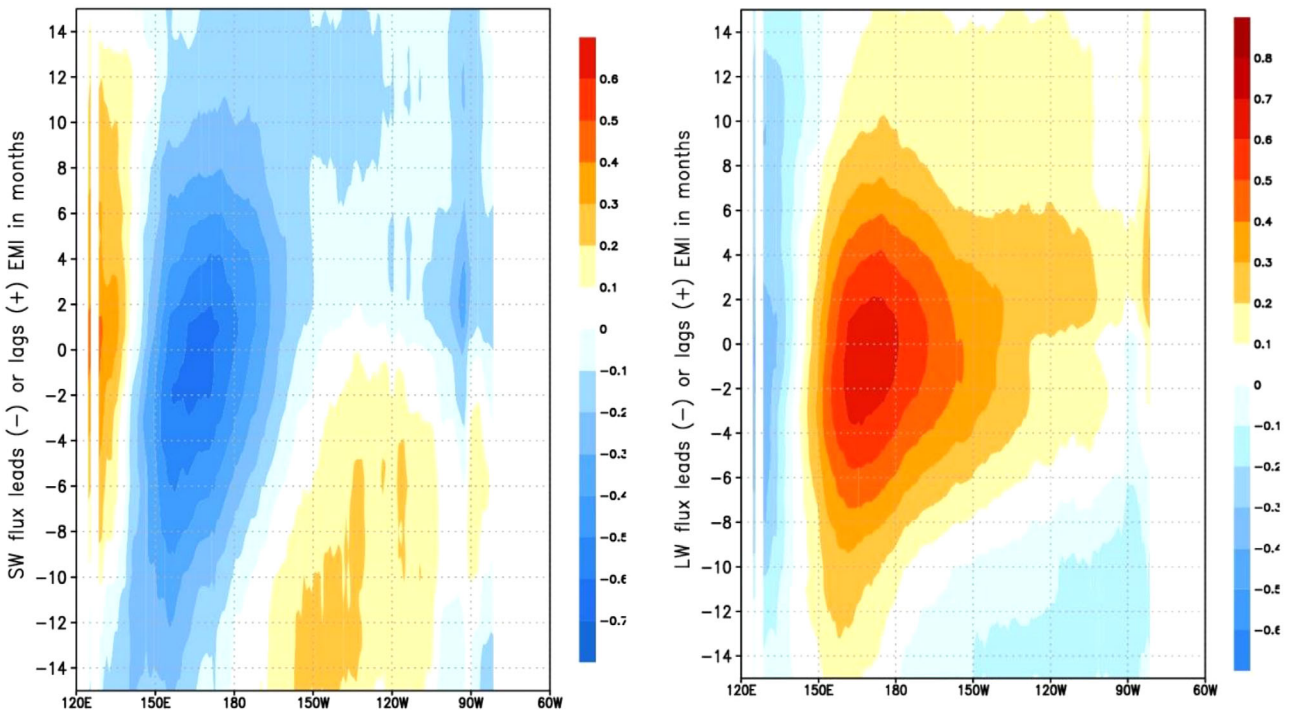

Figure 11. Lag cross correlations between the Modoki Index (EMI) and SW↓ and LW↓ radiative fluxes during the period July 1983 to December 2012 along the equator.

our study investigates the impact of ENSO on SW↓ and LW↓ radiative flux components over the Pacific Ocean during its full cycle. As already recognized by *Klein and Hartmann* [1993], the dominant effect of clouds on earth's climate is via the impact on radiative fluxes. In particular, they recognize a large sensitivity to low clouds of stratocumulus type that tend to form on the east side of the oceanic subtropical highs, over regions of the relatively cold sea surface. In our study, this would be the "cold tongue" area off the coast of Peru. The need for good quality information on ENSO impacts on the radiative forcing functions in the tropical Pacific has been also highlighted by recent attention to the link between the Walker Circulation and possible climate change [*Intergovernmental Panel on Climate Change* (*IPCC*), 2013; *Vecchi et al.*, 2006]. As also stated in *Klein and Hartmann* [1993], a relative increase by 20% in low clouds could balance the greenhouse warming expected from a doubling of carbon dioxide.

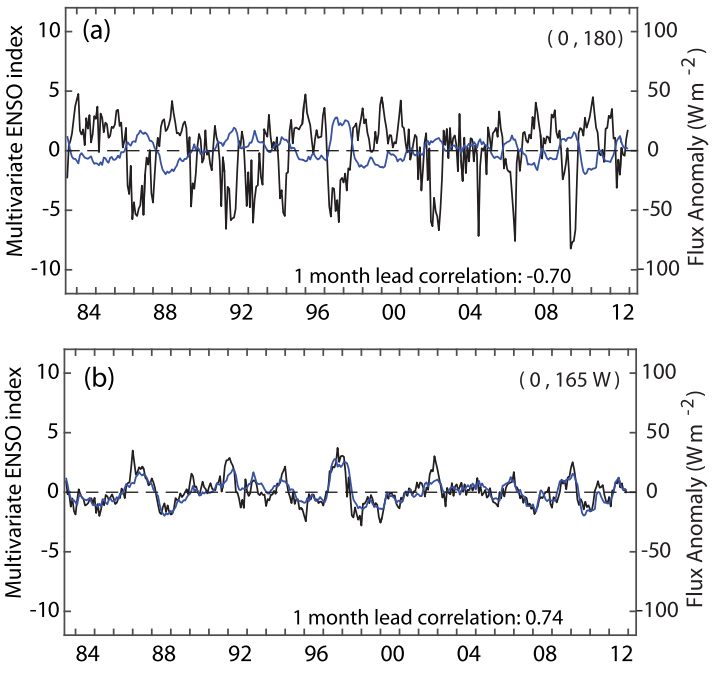

Figure 12. (top) Detrended time series of UMD/SRB SW↓ flux anomalies (black) and Niño3 Index (blue) and (bottom) same as above for LW↓.

Various studies looked at different aspects of the relationship between ENSO and radiative fluxes, both in models and in observations. *Radley et al.* [2014] used observations and four Geophysical Fluid Dynamics Laboratory (GFDL) Atmospheric and

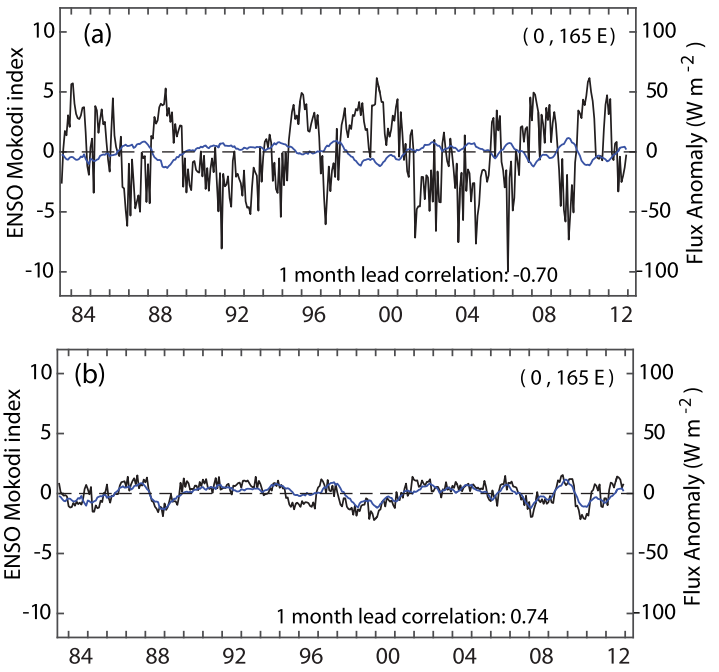

Figure 13. (top) Detrended time series of UMD/SRB SW↓ flux anomalies (black) and EMI Index (blue) and (bottom) same as above for LW↓.

Oceanic General Circulation Models (GCMs) (AGCM) and two independent space observations from the Earth Radiation Budget Experiment (ERBE) and from the Clouds and the Earth's Radiant Energy System (CERES) missions of Outgoing Longwave Radiation (OLR) and SW radiation over the period 1979–2008 to analyze the relation between variations in spatial patterns and area-averaged quantities in the Top-of-the-Atmosphere radiative fluxes, cloud amount, and precipitation related to El Niño. They conclude that models consistently have larger regional anomalies than seen in observations. In our study, we have found that for surface radiative fluxes, reanalyses had smaller anomalies than observations.

Pavlakis et al. [2007, 2008] studied the spatial and temporal variation of surface LW↓ and SW↓ radiation over a 21 year period in the tropical and subtropical Pacific Ocean (40°S–40°N, 90°E–75°W) using monthly mean satellite data from ISCCP-D2 database [*Rossow and Schiffer*, 1999]. A high correlation was found between the LW↓ radiation anomaly and the Niño3.4 index time series, over the Niño3.4 region located in the central Pacific. A high anticorrelation was also found over the western Pacific (150°S–0°S, 105°E–130°E). They report that there is evidence that the time series of the mean LW↓ anomaly in the western Pacific precedes that in the Niño3.4 region by 3–4 months. Over the Niño3.4 region, the mean LW↓ anomaly values range from $+20$ W m^{-2} during El Niño episodes to -20 W m^{-2} during La Niña events, while over the western Pacific (15°S–0°S, 105°E–130°E) these values range from -15 to $+10$ W m^{-2}, respectively. We find much larger anomalies in LW↓ fluxes than reported in their study. A clear anticorrelation was found between SW↓ radiation anomaly time series, in the region 7°S–5°N, 160°E–160°W located west of the Niño3.4 region, and the Niño3.4 index time series. They report that the highest value of SW↓ anomaly was in the range of -45 W m^{-2} during El Niño episodes to $+40$ W m^{-2} during La Niña events. There is also convincing evidence that the time series of the mean downward SW↓ anomaly in the off-equatorial western Pacific region 7°N–15°N, 150°E–170°E, precedes the Niño 3.4 index time series by about 7 months and the pattern of this anomaly is indicative of ENSO operating through the mechanism of the western Pacific oscillator. We find much larger anomalies in SW↓ fluxes than reported in their study. Possible explanation for such differences can be related to basic differences in the version of the ISCCP data used in these studies. *Pavlakis et al.* [2007, 2008] used the ISCCP D2 version which are monthly mean averages over a 2.5° grid. The ISCCP DX (used in this study) are 3 hourly pixel level data that have been gridded to 0.5° resolution. Due to the nonlinearity in the radiative flux computations, the ISCCP D2 based results would be different than those that are computed at 3 hourly time scale at 0.58 resolution (showing less variability).

Sandeep et al. [2014] used observational and reanalysis data and coupled (atmosphere-ocean) as well as uncoupled (atmosphere only, prescribed SST) model simulations to investigate twentieth century changes in the tropical Pacific Walker Cell (PWC) and their physical mechanisms. Based on their results, they challenge the notion that a weakening or strengthening PWC trend is strongly tied to a weakening or strengthening of the global convective mass flux. They also point out that the reanalysis data could be affected by the quality of the observations that are assimilated. They suspect that the weakening of

the PWC trend obtained in the Coupled Model Intercomparison Project Phase 5 (CMIP5) [*IPCC*, 2013] is ultimately due to miss-representation and systematic underestimation of the spatial variation of tropical SST trends.

Bayer et al. [2014] also discuss the eastward shift of the Walker Circulation in response to global warming and its relationship to ENSO variability. They conclude that two thirds of the global warming forced trend of the Walker Circulation can be explained by a long-term trend in the interannual variability pattern, namely, a shift toward more El Niño-like conditions in the multimodel mean, under global warming.

Sohn et al. [2013] use satellite observations to show that there is evidence for the claim of strengthening of the PWC circulation. It is based on three decades of the microwave Special Sensor Microwave Imager (SSM/I) measurements of the water budget. They use satellite and surface observations to examine whether they agree with a working hypothesis of intensified Walker Circulation. They conclude that the 30 year analysis period is too short to discuss whether the observed strengthened Walker Circulation is due to global warming or natural variation in the Earth-Atmosphere climate system, independent of the warming trend.

Bellenger et al. [2014] analyzed the ability of CMIP models to simulate the observed nonlinearity of the shortwave feedback which arises because the real atmosphere switches from subsiding to convective regimes under the effect of seasonal and interannual variations. Since only one third of CMIP3 + CMIP5 models reproduced the regime shift, it was suggested that an improved mean state would lead to an improved shortwave feedback nonlinearity.

In this study, we have documented the impact of El Niño and La Niña cycles on the surface radiative fluxes and investigated the correlations between their anomalies and various El Niño indices. We have also investigated the surface wind divergence/convergence to shed light on the issue of causes for limiting eastward excursions of convection. We found that the main factor limiting eastward excursions of convection is the surface wind convergence. Due to the wind divergence pattern normally present over the eastern cold tongue, anomalous convection extends into the eastern equatorial Pacific only during the strongest warm events. For the traditional eastern Pacific ENSO, the maximum variance of anomalous incoming solar radiation (SW↓) is located just west of the dateline and is coincident with the area of anomalous SST gradient. Anomalous SW↓ reaches ~60 W/m^2 in magnitude and lags behind the Niño3 index, suggesting that it responds to anomalous SST. In contrast, the LW↓ anomaly magnitude is half that strong. It is spatially coherent and varies in phase with SST anomaly. Our analysis also considers the El Niño Modoki events, for which the radiation flux patterns are shifted westward following the Modoki SST pattern. We have established that reanalysis products are not fully able to reproduce observed patterns of ENSO-related radiative flux variability. While deficiencies of climate models in respect to ENSO have been discussed previously [e.g., *Trenberth et al*., 2010] they conducted comparisons of radiation parameters at the Top-of-the-Atmosphere. As explained by *Mayer et al*. [2016], the differences at that level are due to strongly biased responses of net radiation at Top-of-the-Atmosphere to ENSO because of biases of mean convective activity in the models. The analysis at the surface adds a dimension for the understanding of differences between models and observations. In this study, it was demonstrated that among the reanalyses investigated, the ENSO evolution was best captured by the ERA-I model as compared to observations. We find that the observational anomalies during El Niño and La Niña are stronger than in the reanalyses; for instance, the original anomaly in SW↓ over the warm pool region can be as high as 60 W m^{-2}, it propagates westward and can reach similar intensity. Corresponding values in LW↓ are about 35 W m^{-2}. Tropical convection onset, which governs cloud cover and incoming solar radiation, requires both SST $>$ 27.5°C along with surface wind convergence, divU $<$ 0, to maintain atmospheric updraft [*Graham and Barnett*, 1987]. Under normal conditions, divU $>$ 0 in the east over cool SST of the cold tongue. Because SST increases westward and divU $>$ 0 over the cold tongue water, the convection should occur where both, SST $>$ 27.5°C and divU $<$ 0. From Figure 7, we may conclude that deep convection in the equatorial Pacific is limited by wind divergence rather than SST. Our paper focuses on interannual fluctuations of the tropical Pacific downwelling SW↓ predominantly forced by ENSO. These interannual fluctuations occur on the background of longer-term changes, in part forced by more rapid warming of the tropical Indian Ocean in comparison with the tropical Pacific. According to *Zhang and Karnauskas* [2017], this long-term interbasin SST contrast contributes to strengthening La Nina pattern in the Pacific. But these longer-term changes could not be resolved well in our study due to limited span of time records.

Appendix A: Methodology to Homogenize Independent Satellite Data

Evaluation of the ISCCP DX data over oceans [*Ma and Pinker*, 2012] shows that the satellite-based retrievals tend to overestimate the SW↓ irradiance over oceans (not so over land). In particular, large differences have been documented over the Atlantic Ocean. Evaluation of SW↓ fluxes as derived from the Moderate Resolution Imaging Spectroradiometer (MODIS) observations [*King et al.*, 1992, 2003] against the same oceanic arrays as used for the evaluation of the ISCCP DX data, are described in *Pinker et al.* [2009]; they show good agreement between the estimates and the observations. We have computed anomalies in the MODIS based estimates using multiyear monthly mean radiative flux data, generating the mean annual cycle by averaging the monthly fluxes for the same month each year. The departure from the mean annual cycle (anomalies) from these two data sources are illustrated in Figure A1a based on global scale observations. Subsequently, the biases in the ISCCP DX fluxes were adjusted according to the MODIS observations. To make correction to daily SW↓ fluxes, the bias was normalized by top of atmosphere daily shortwave down flux. These corrected data sets (after bias removal) are being used in this study. In Figure A1b, we show the departures from the mean annual cycle for the tropical Pacific belt of 20°S–20°N after bias removal. As evident, no marked inconsistency is evident in respect to the characteristic magnitude of the ENSO signal which exceeds several tens of W/m^2. The same was done for the LW↓ fluxes, however, the differences in anomalies were not as large as in the case of SW↓ fluxes. This bias removal led to improvement in satellite estimates when compared to the BSRN observations as well as against the TOA/TRITON array of buoys [*McPhaden et al.*, 1998], as shown in Figure A2.

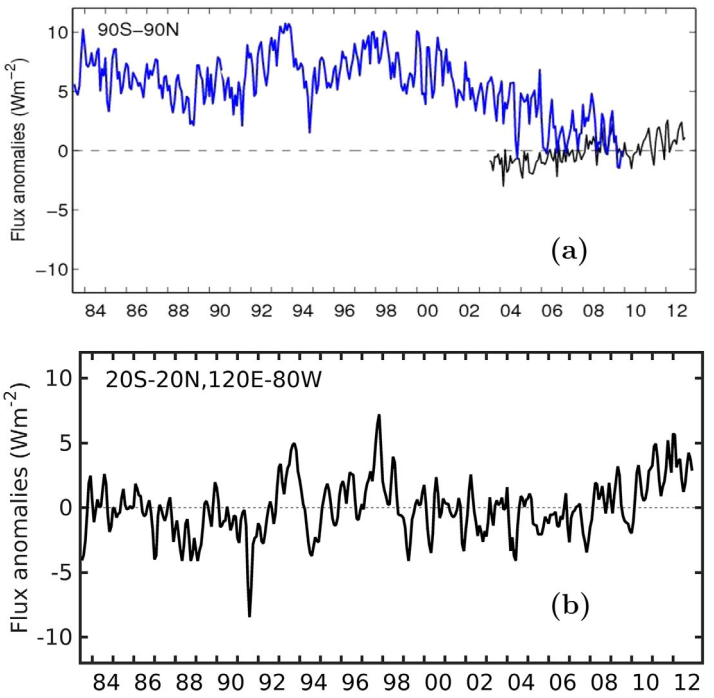

Figure A1. (a) Time series of global scale monthly mean anomalies from UMD_ISCCP DX SW↓ (*blue*) and UMD_MODIS_SW↓ (*black*) after removing the seasonal cycle; (b) illustrating the homogeneity of the data over the tropical Pacific belt of 20°S–20°N after bias removal; three point smoothing with weights 1, 2, and 1 was used.

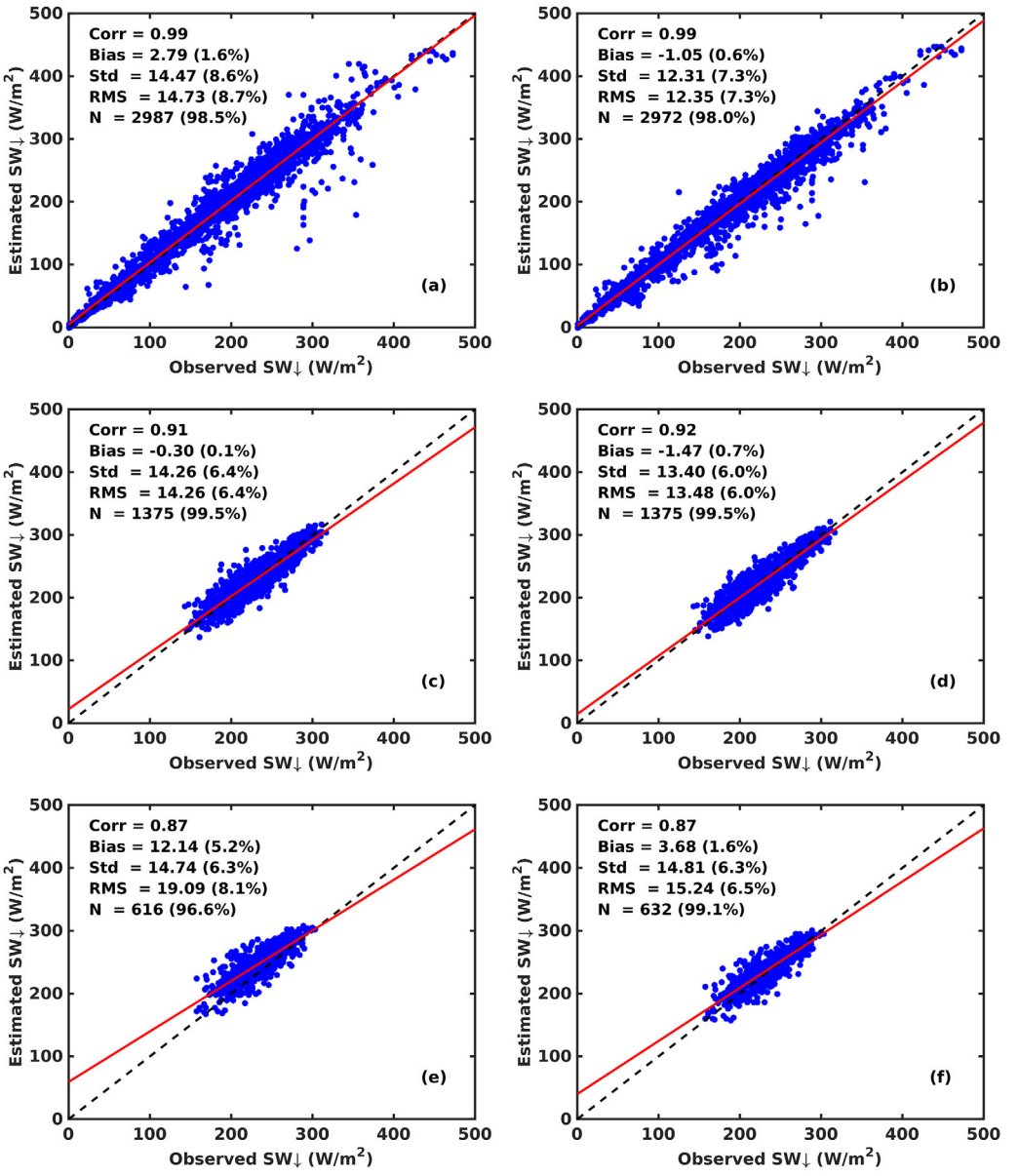

Figure A2. Evaluation of satellite and model estimates of surface SW at monthly time scale. (a) DX without Bias correction against BSRN (1992–2009), (b) MODIS (new) against BSRN (1992–2009), (c) DX without Bias correction against TAO (2000–2009), (d) MODIS (new) against TAO (2000–2009), (e) DX without Bias correction against PIRATA (2000–2009), and (f) MODIS (new) against PIRATA (2000–2009).

Acknowledgments

The analysis was completed under NASA grant NNX13AC12G, the Energy and Water Cycle Study (NEWS) program. The work benefited from support under NASA grant NNX08AN40A from the Science Mission Directorate-Division of Earth Science. Thanks are due to the NASA GES DISC Giovanni for the MODIS data, to the various MODIS teams that produced data used in this study, and to the NASA Langley Research Center Atmospheric Science Data Center for providing the ISCCP DX data. We acknowledge the TAO Project Office of NOAA/PMEL for providing data from the Tropical Atmosphere Ocean/ Triangle Trans-Ocean Buoy Network (TAO/TRITON) and from the Pilot Research Moored Array in the Tropical Atlantic (PIRATA) moorings in the tropical Atlantic that were used in this study. We acknowledge the ECMWF for providing the ERA-I data; the MERRA-2 data are provided by the Global Modeling and Assimilation Office (GMAO), NASA/GSFC; the Japan Meteorological Agency (JMA) provided the JRA55 data; and NCEP Reanalysis data are provided by the NOAA/OAR/ ESRL PSD, Boulder, Colorado, USA. The radiative fluxes used in this study are located at: http://www.aosc.umd.edu/ ~srb/NEWS/webNEWS.htm. We are grateful to two anonymous reviewers for very helpful and constructive comments and to the Editor for overseeing the disposition of this manuscript.

References

Ashok, K., and T. Yamagata (2009), The El Niño with a difference, *Nature*, *461*, 481–484.

Ashok, K., S. K. Behera, S. A. Rao, H. Weng, and T. Yamagata (2007), El Niño Modoki and its possible teleconnection, *J. Geophys. Res.*, *112*, C11007, doi:10.1029/2006JC003798.

Bayer, T., D. Dommenget, T. Martin, and S. B. Power (2014), The eastward shift of the Walker Circulation in response to global warming and its relationship to ENSO variability, *Clim. Dyn.*, *43*, 2747–2763, doi:10.1007/s00382-014-2091-y.

Bellenger, H., E. Guilyardi1, J. Leloup, M. Lengaigne, and J. Vialard (2014), ENSO representation in climate models: from CMIP3 to CMIP5, *Clim. Dyn.*, *42*(7–8), 1999–2018.

Berrisford, P., D. Dee, K. Fielding, M. Fuentes, P. Kållberg, S. Kobayashi, and S. Uppala (2009), *The ERA-Interim Archive, Version 1.0, ERA Rep. Ser. 1*, Eur. Cent. for Medium-Range Weather Forecasts, Reading, U. K.

Bosilovich, M. G., et al. (2015), MERRA-2: Initial evaluation of the climate, in *Technical Report Series on Global Modeling and Data Assimilation*, vol. 43, *Rep. NASA/TM–2015–104606*, edited by R. D. Koster. [Available at https://gmao.gsfc.nasa.gov/pubs/docs/Bosilovich803.pdf.]

Dee, D. P., et al. (2011), The ERA-Interim reanalysis: Configuration and performance of the data assimilation system, *Q. J. R. Meteorol. Soc.*, *137*, 553–597, doi:10.1002/qj.828.

Desbiolles, F., A. Bentamy, B. Blanke, A. M. Mestas-Nuñez, S. A. Grodsky, S. Herbette, C. Roy, G. Cambon, and C. Maes (2017), Two decades (1992–2012) of surface wind analyses based on satellite scatterometer observations, *J. Mar. Syst.*, *168*, 38–56, doi:10.1016/j.jmarsys.2017.01.003.

Gill, A. E. (1980), Some simple solutions for heat-induced tropical circulation, *Q. J. R. Meteorol. Soc.*, *106*, 447–462, doi:10.1002/qj.49710644905.
Graham, N. E., and T. P. Barnett (1987), Sea surface temperature, surface wind divergence, and convection over tropical oceans, *Science*, *238*, 657–659, doi:10.1126/science.238.4827.657.
Grodsky, S. A., A. Bentamy, J. A. Carton, and R. T. Pinker (2009), Intra-seasonal latent heat flux based on satellite observations, *J. Clim.*, *22*, 4539–4556, doi:10.1175/2009JCLI2901.1.
Hall, A., and S. Manabe (2000), Effect of water vapor feedback on internal and anthropogenic variations of the global hydrologic cycle, *J. Geophys. Res.*, *105*(D5), 6935–6944.
Intergovernmental Panel on Climate Change (IPCC) (2013), Climate Change 2013: The physical science basis, in *Contribution of Working Group I to the Fifth Assessment Report of the Intergovernmental Panel on Climate Change*, edited by T. F. Stocker et al., Cambridge Univ. Press, Cambridge, U. K. [Available at http://www.ipcc.ch/.]
Kalnay, E., et al. (1996), The NCEP/NCAR 40-Year Reanalysis Project, *Bull. Amer. Meteorol. Soc.*, *77*, 437–471, doi:10.1175/1520-0477(1996)077 < 0437:TNYRP>2.0.CO;2.
King, M. D., Y. J. Kaufman, W. P. Menzel, and D. Tanre (1992), Remote sensing of cloud, aerosol, and water vapor properties from the Moderate Resolution Imaging Spectrometer (MODIS), *IEEE Trans. Geosci. Remote Sens.*, *30*, 2–27, doi:10.1109/36.124212.
King, M. D., et al. (2003), Cloud and aerosol properties, perceptible water, and profiles of temperature and humidity from MODIS, *IEEE Trans. Geosci. Remote Sens.*, *41*, 442–458, doi:10.1109/TGRS.2002.808226.
Klein, S. A., and D. L. Hartmann (1993), The seasonal cycle of low stratiform clouds, *J. Clim.*, *6*(8), 1587–1606.
Klein, S. A., B. J. Soden, and N. C. Lau (1999), Remote sea-surface temperature variations during ENSO: Evidence for a tropical atmospheric bridge, *J. Clim.*, *12*, 917–932.
Kobayashi, S., et al. (2015), The JRA-55 reanalysis: General specifications and basic characteristics, *J. Meteorol. Soc. Jpn.*, *93*(1), 5–48, doi:10.2151/jmsj.2015-001.
Lindzen, R., and S. Nigam (1987), On the role of sea surface temperature gradients in forcing low-level winds and convergence in the tropics, *J. Atmos. Sci.*, *44*, 2418–2436, doi:10.1175/1520-0469(1987)044 < 2418:OTROSS>2.0.CO;2.
Ma, Y., and R. T. Pinker (2012), Modeling shortwave radiative fluxes from satellites, *J. Geophys. Res.*, *117*, D23202, doi:10.1029/2012JD018332.
Mayer, M., J. T. Fasullo, K. E. Trenberth, and L. Haimberger (2016), ENSO-driven energy budget perturbations in observations and CMIP models, *Clim. Dyn.*, *47*, 4009–4029, doi:10.1007/s00382-016-3057-z.
McPhaden, M. J., et al. (1998), The Tropical Ocean-Global Atmosphere observing system: A decade of progress, *J. Geophys. Res.*, *103*(C7), 14,169–14,240, doi:10.1029/97JC02906.
Nussbaumer, E. A., and R. T. Pinker (2012), Estimating surface longwave radiative fluxes from satellites utilizing artificial neural networks, *J. Geophys. Res.*, *117*, D07209, doi:10.1029/2011JD017141.
Oort, A. H., and J. J. Yienger (1996), Observed inter-annual variability in the Hadley Circulation and its connection to ENSO, *J. Clim.*, *9*, 2751–2767.
Pavlakis, K. G., D. Hatzidimitriou, E. Drakakis, C. Matsoukas, A. Fotiadi, N. Hatzianastassiou, and I. Vardavas (2007), ENSO surface longwave radiation forcing over the tropical Pacific, *Atmos. Chem. Phys.*, *7*, 2013–2026.
Pavlakis, K. G., N. Hatzianastassiou, C. Matsoukas, A. Fotiadi, and I. Vardavas (2008), ENSO surface shortwave radiation forcing over the tropical Pacific, *Atmos. Chem. Phys.*, *8*, 5565–5577.
Philander, S. G. (1990), *El Niño, La Niña, and the Southern Oscillation*, 289 pp., Academic, London.
Pinker, R. T., H. Wang, and S. A. Grodsky (2009), How good are ocean buoy observations of radiative fluxes?, *Geophys. Res. Lett.*, *36*, L10811, doi:10.1029/2009GL037840.
Radley, C., S. Fueglistaler, and L. Donner (2014), Cloud and radiative balance changes in response to ENSO in observations and models, *J. Clim.*, *27*, 3100–3113, doi:10.1175/JCLI-D-13-00338.1.
Rasmusson, E. M., and T. H. Carpenter (1982), Variations in tropical sea surface temperature and surface wind fields associated with the Southern Oscillation El Nino, *Mon. Weather Rev.*, *110*(5), 354–384, doi:10.1175/1520-0493.
Reynolds, R. W., N. A. Rayner, T. M. Smith, D. C. Stokes, and W. Wang (2002), An improved in situ and satellite SST analysis for climate, *J. Clim.*, *15*, 1609–1625.
Rodriguez-Puebla, C., R. T. Pinker, and S. Nigam (2008), Relationship between downwelling surface shortwave radiative fluxes and sea surface temperature over the tropical Pacific: AMIP II models versus satellite estimates, *Ann. Geophys.*, *26*, 785–794.
Rossow, W. B., and R. A. Schiffer (1991), ISCCP cloud data products, *Bull. Am. Meteorol. Soc.*, *72*, 2–20, doi:10.1175/1520-0477(1991)072 < 0002:ICDP>2.0.CO;2.
Rossow, W. B., and R. A. Schiffer (1999), Advances in understanding clouds from ISCCP, *Bull. Am. Meteorol. Soc.*, *80*, 2261.
Sandeep, S., F. Stordal, P. D. Sardeshmukh, and G. P. Compo (2014), Pacific Walker Circulation variability in coupled and uncoupled climate models, *Clim. Dyn.*, *43*(1), 103–117.
Simmons, A., S. Uppala, D. Dee, and S. Kobayashi (2007), ERA-Interim: New ECMWF reanalysis products from 1989 onwards, *ECMWF Newslett.*, 110, 25–35.
Sohn, B. J., S.-W. Yeh, J. Schmetz, and H.-J. Song (2013), Observational evidences of Walker Circulation change over the last 30 years contrasting with GCM results, *Clim. Dyn.*, *40*, 1721–1732, doi:10.1007/s00382-012-1484-z.
Trenberth, K. E. (1997), The definition of El Nino, *Bull. Am. Meteorol. Soc.*, *78*(12), 2771–2777.
Trenberth, K. E., and T. J. Hoar (1996), El Niño and climate change, *Geophys. Res. Lett.*, *24*(23), 3057–3060.
Trenberth, K. E., J. T. Fasullo, C. O'Dell, and T. Wong (2010), Relationships between tropical sea surface temperature and top-of-atmosphere radiation, *Geophys. Res. Lett.*, *37*, L03702, doi:10.1029/2009GL042314.
Vecchi, G. A., B. J. Sode., A. T. Wittenberg, I. M. Held, A. Leetmaa, and M. J. Harrison (2006), Weakening of tropical Pacific atmospheric circulation due to anthropogenic forcing, *Nature*, *441*(7089), 73–76, doi:10.1038/nature04744.
Wang, H., and R. T. Pinker (2009), Shortwave radiative fluxes from MODIS: Model development and implementation, *J. Geophys. Res.*, *114*, D20201, doi:10.1029/2008JD010442.
Wolter, K., and M. S. Timlin (2011), El Niño/Southern Oscillation behaviour since 1871 as diagnosed in an extended multivariate ENSO index (MEI.ext), *Int. J. Climatol.*, *31*, 1074–1087, doi:10.1002/joc.2336.
Yau, M. K., and R. R. Rogers (1989), *Short Course in Cloud Physics*, 3rd ed., 304 pp., Butterworth-Heinemann, Oxford, U. K.
Yeh, S.-W., J.-S. Kug, B. Dewitte, M.-H. Kwon, B. P. Kirtman, and F.-F. Jin (2009), El Niño in a changing climate, *Nature*, *461*, 511–514, doi:10.1038/nature08316.
Zhang, L., and K. B. Karnauskas (2017), The role of tropical interbasin SST gradients in forcing walker Circulation trends, *J. Clim.*, *30*(2), 499–508, doi:10.1175/JCLI-D-16-0349.1.